J Mater Sci (2010) 45:151–157
DOI 10.1007/s10853-009-3910-0

Fabrication and characterization of ferroelectric PLZT film capacitors on metallic substrates

Beihai Ma · Manoj Narayanan · Sheng Tong · U. Balachandran

Received: 20 August 2009 / Accepted: 17 September 2009 / Published online: 30 September 2009

Abstract We have grown ferroelectric $Pb_{0.92}La_{0.08}Zr_{0.52}Ti_{0.48}O_3$ (PLZT) films on Hastelloy C276 (HC) substrates by chemical solution deposition. Samples of 1.15-μm-thick PLZT films were prepared on HC with and without lanthanum nickel oxide (LNO) films as an intermediate buffer layer. On samples with and without LNO buffers at room temperature, we measured dielectric constants of ≈1,300 and ≈450 and loss tangents of ≈0.06 and ≈0.07, respectively. For PLZT films grown on HC with LNO buffer, the dielectric constant increases, while the dielectric loss decreases, with increasing temperature. A dielectric constant of ≈2,000 and loss of ≈0.05 were observed at 150 °C. Samples with LNO buffer also exhibited slimmer hysteresis loops and lower leakage current density when compared to samples without LNO buffer. The following results were measured on samples with and without LNO buffers: remanent polarization (P_r) values of 21.3 and 36.4 μC/cm^2, coercive electric field (E_c) values of 41 and 173 kV/cm, and leakage current densities of ≈1.1 × 10^{-8} and ≈1.6 × 10^{-7} A/cm^2, respectively. The energy storage capability was measured at ≈65 J/cm^3 for the PLZT film-on-foil capacitor deposited on HC with LNO buffer.

Introduction

In recent years, interest in the development of ferroelectric (FE) thin films has intensified because of the anticipated applications for decoupling capacitors, micro-actuators, electro-optical components, and digital memories [1–5]. Applications are also feasible in advanced power electronics, which require capacitors that are capable of operating under high voltage and yet have minimal footprint. This requirement can be fulfilled by stacking or embedding high-permittivity ceramic film capacitors into a printed circuit board (PCB). Technology development in this area would free up surface space, reduce the number of solder joints on the PCB, and therefore, lead to increased device reliability and minimization of electromagnetic interference and inductance loss. Although the technology has primarily received attention for decoupling capacitors in microelectronic applications, it can potentially be extended to high-power applications, such as plug-in hybrid electric vehicles. At present, the integration of high-permittivity films into PCBs is a challenge because of the incompatibility in the processing conditions for the different materials involved. Polymer layers in a PCB cannot withstand the high temperatures (600–700 °C) required for tailoring the ceramic film dielectrics to the desired crystalline structures. Development of these crystalline structures is extremely difficult at reduced processing temperatures [6]. Success has been demonstrated through a film-on-foil approach, where the ceramic dielectrics are first coated on a thin base metal foil by chemical solution deposition and then crystallized at high temperature [5, 7, 8]. These coated foils can subsequently be embedded into a PCB.

By far, the vast majority of FE films are fabricated on single crystals or silicon wafers [3, 9–11]. Use of metallic substrates, however, is potentially beneficial for the fabrication of large-area devices with low cost. Metal foils coated with dielectric material, the so-called "film-on-foil dielectric sheets," could be laminated onto PCBs to create embedded capacitors that have broad applications in power electronics. Or, these film-on-foils could be stacked to form a capacitor cartridge with minimal footprint on a circuit

B. Ma (✉) · M. Narayanan · S. Tong · U. Balachandran
Energy Systems Division, Argonne National Laboratory, Argonne, IL 60439, USA
e-mail: bma@anl.gov

board. However, substantial technical challenges still exist in the fabrication of FE film-on-foil capacitors that exhibit high dielectric strength and are crack free. Problems include thermal expansion mismatch between films and metal substrates, formation of a low-dielectric-constant parasitic layer at the film/substrate interface, and diffusion of cations from the substrate into the dielectric film.

We earlier reported [12–14] fabrication of high-energy–density FE $Pb_{0.92}La_{0.08}Zr_{0.52}Ti_{0.48}O_3$ (PLZT) film-on-foil capacitors on base metal (nickel and copper) sheets. To produce film-on-foil sheets with high quality, we found it necessary to apply a conductive oxide buffer to the nickel foil prior to the deposition of PLZT. This architecture allows crystallization of dielectric ceramic films grown on nickel foils directly in air without the formation of deleterious interfacial secondary phases [12, 13]. An alternative approach is to anneal the ceramic dielectric films in a controlled atmosphere with reduced oxygen partial pressure [14]. Seifert et al. [15] reported the deposition of lead zirconate titanate (PZT, 53/47) on Hastelloy C276 (HC) foils with lanthanum strontium manganate buffer layer. In this article, we report our recent studies on the fabrication of FE PLZT (8/52/48) films by chemical solution deposition on HC foils with and without lanthanum nickel oxide (LNO) buffer. This particular alloy was selected as a substrate because of its superior strength for easy handling and its thermal and chemical stability, which are advantageous for high temperature processing of film-on-foil dielectric sheets. The FE PLZT film-on-foil capacitors grown on LNO buffered HC substrates exhibit high breakdown field strength [12] and, therefore, are extremely promising for high-power energy storage.

Experimental procedure

Hastelloy C-276 foils $\approx$100 μm in thickness were obtained from IGC-SuperPower, LLC (Schenectady, NY). The foils were electropolished. A root-mean-square (RMS) surface roughness of $\approx$2 nm was measured by atomic force microscopy (AFM) in the tapping mode with 5 × 5 μm scan size. Substrates of 10 × 10 mm were cut from the received foils. Prior to being coated, these substrates were ultrasonically cleaned in distilled water, and then wiped clean with acetone and methanol in sequence. Two types of samples, with and without LNO buffer, were deposited on HC substrates.

Precursor solutions (0.2 M) of LNO ($LaNiO_3$) were prepared by dissolving an appropriate amount of lanthanum nitrate and nickel acetate in 2-methoxyethanol and refluxing for 2 h inside a chemical glove box. Precursor solutions (0.5 M) of PLZT were prepared by a modified 2-methoxyethanol synthesis route [16, 17] using an appropriate amount of lead acetate trihydrate, titanium isopropoxide, zirconium *n*-propoxide, and lanthanum nitrate. The resulting solution contains 20% excess lead to compensate for the loss during the heat treatment described below. Before being used for coating, the LNO and PLZT precursor solutions were filtered through Whatman (Whatman Inc., Sanford, ME) syringe filters of 0.02-μm pore size. The filtered LNO precursor solution was spin coated with a Laurell WS400 spin processor (Laurell Technologies, North Wales, PA) at 3,000 rpm for 30 s on HC substrates, pyrolyzed at 450 °C for 5 min, and annealed at 625 °C for 2–5 min in air. This process was repeated three times to build the desired $\approx$0.4-μm-thick LNO buffer film. For samples without the LNO buffer, filtered PLZT precursor solution was spin coated directly on HC substrates at 3,000 rpm for 30 s. For samples with the LNO buffer, filtered PLZT precursor solution was spin coated on LNO-buffered HC substrates at 3,000 rpm for 30 s. For samples with and without the LNO buffer, pyrolysis was at 450 °C for 5 min with subsequent annealing at 650 °C for 5–10 min for each coating of PLZT. After every three layers of coating, additional annealing was performed at 650 °C for 15 min. Solution coating and firing were repeated to produce films of desired thickness. All pyrolysis and annealing were performed in air in Lindburg tube furnaces. Each coating resulted in a PLZT film of $\approx$0.115-μm thickness after pyrolysis and crystallization. Film thickness was determined from cross-sectional images with scanning electron microscopy (SEM) [17].

The phase development in the processed films was studied by a Bruker AXS D8 diffraction system. Their microstructures were characterized by a Hitachi S-4700-II field-emission electron microscope. The surface roughness of the films was measured by a Veeco Instruments D3100 scanning probe microscope operated in the tapping mode.

Platinum (Pt) top electrodes with thickness of 100 nm were deposited by electron-beam evaporation through a shadow mask to define $\approx$250-μm-diameter capacitors. Samples with Pt top electrodes were annealed at 450 °C in air for 2 min for electrode conditioning. A Signatone QuieTemp® probe system with heatable vacuum chuck (Lucas Signatone Corp., Gilroy, CA) was used for electrical characterization. For the electrical measurements, the Pt/PLZT(/LNO)/HC heterostructure was contacted by a Pt top electrode pad with one probe and the HC substrate (bottom electrode) with the other. A positive applied voltage corresponds to the configuration where the top electrode is at a higher potential than the bottom electrode. As illustrated in Fig. 1, probe 1 is at a higher potential than probe 2 when a positive bias voltage is applied, whereas probe 1 is at a lower potential when a negative bias voltage is applied. An HP 4192A impedance analyzer measured the capacitance and dissipation factor under ±35 V applied bias field. A Radiant Technologies' Precision Premier II

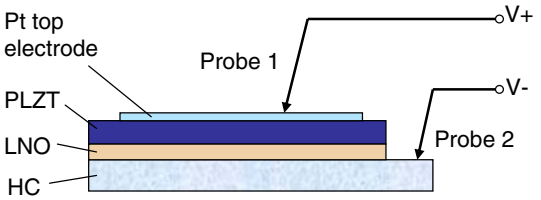

Fig. 1 Schematic illustration of electrical testing setup for the film-on-foil capacitors

tester measured the hysteresis loops. The samples were immersed in silicon oil during the high-field hysteresis measurements. A Keithley 237 high-voltage source meter measured the current–voltage characteristics. The leakage current density was determined by fitting the current density relaxation data to the Curie–von Schweidler equation [18]. Data were collected with a computer whose internal clock was used for recording the time of the relaxation process.

Results and discussion

Figure 2a shows AFM images of the top surface of a ≈1.15-μm-thick PLZT film grown on a HC substrate with LNO buffer, hereafter referred to as "PLZT/LNO/HC" sample. Figure 2b presents an AFM image of a ≈1.15-μm-thick PLZT film grown on HC substrate without LNO buffer ("PLZT/HC" sample).

The PLZT/LNO/HC sample is dense and uniform; no porosity or cracks are evident (Fig. 2a). The average grain size is ≈60 nm. Besides allowing the PLZT film-on-foil capacitors to be processed in air without the formation of a parasitic secondary-phase interfacial layer, the LNO buffer was expected to compensate for the roughness of the metal foil (RMS value of ≈2 nm) and provide a smoother surface for the PLZT films to grow on, resulting in higher breakdown strengths. Additionally, the LNO buffer was expected to reduce the compressive strain in the PLZT films deposited directly on HC substrates due to the thermal expansion coefficient mismatch between PLZT and metal substrates [19].

The PLZT/HC sample is also dense and absent of cracks (Fig. 2b). Different surface morphology was observed when compared with the PLZT/LNO/HC sample. The feature near the center of the AFM image in Fig. 2b is likely associated with a secondary phase.

Figure 3 shows the X-ray diffraction patterns taken on PLZT/LNO/HC and PLZT/HC samples with Pt top electrodes. Neither sample has a preferred crystallographic orientation. The PLZT films exhibit a perovskite structure with tetragonal distortion. All peaks can be indexed accordingly (JCPDS No. 56-0900). The small peak at

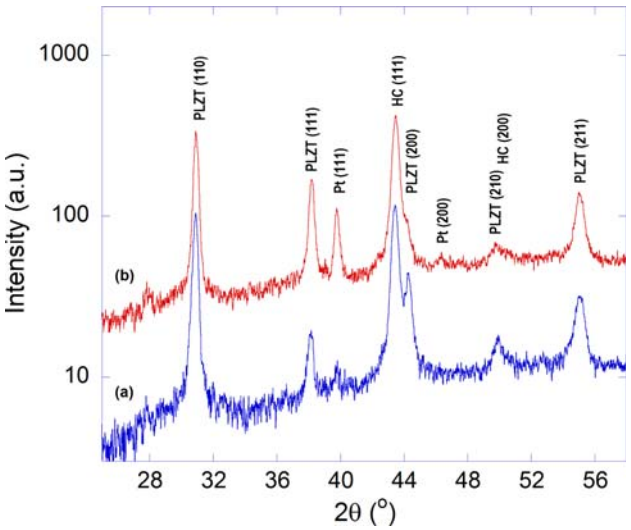

Fig. 3 X-ray diffraction pattern of (*a*) Pt/PLZT/LNO/HC and (*b*) Pt/PLZT/HC samples

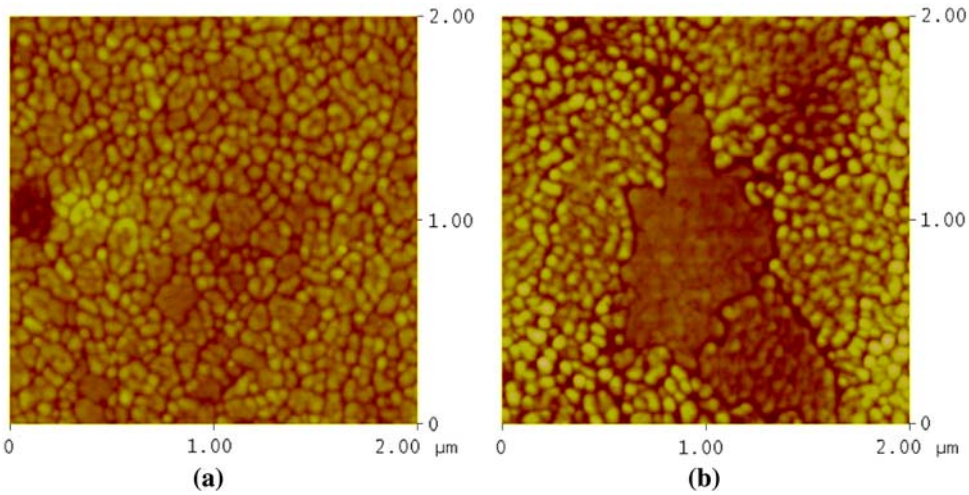

Fig. 2 Atomic force microscopy images of: **a** PLZT/LNO/HC and **b** PLZT/HC samples

$2\theta \approx 28°$ in the diffraction pattern for the Pt/PLZT/HC sample is likely associated with the secondary phase at the PLZT–substrate interface. Further studies are ongoing to identify any secondary phase formed at the interface and the effects on the performance of the film-on-foil capacitors.

Figure 4 shows the dielectric properties of the PLZT/LNO/HC and PLZT/HC samples as a function of applied bias field. These measurements were undertaken at room temperature with a frequency of 10 kHz. At 0-V bias, a dielectric constant of ≈1,300 and dielectric loss of ≈0.06 were measured for the Pt/PLZT/LNO/HC sample, as shown in Fig. 4a; the corresponding values are ≈450 and ≈0.07 for the Pt/PLZT/HC sample, as shown in Fig. 4b. Here we used a simple parallel capacitor model for the calculation of the dielectric constant. These results are comparable to those reported for PLZT grown on nickel substrates with and without LNO buffer [17]. The dielectric tunability, defined as the ratio of the dielectric constant at field E and at zero field $[1 - \varepsilon(E)/\varepsilon(0)]$, was measured at room temperature with an applied field of 200 kV/cm. The tunability results for the PLZT/LNO/HC and PLZT/HC samples were 70% and 40%, respectively.

Figure 5 shows the dielectric properties of PLZT/LNO/HC and PLZT/HC samples measured at room temperature as a function of frequency, respectively. No bias field was applied during the measurement. The dielectric constant decreases and loss increases with increasing frequency from 500 Hz to 1 MHz for the Pt/PLZT/LNO/HC sample, as shown in Fig. 5a. For the Pt/PLZT/HC sample, the dielectric constant and loss both decrease with increasing frequency over the same range, as shown in Fig. 5b.

Figure 6 shows the dielectric properties measured as a function of temperature for the PLZT/LNO/HC and PLZT/

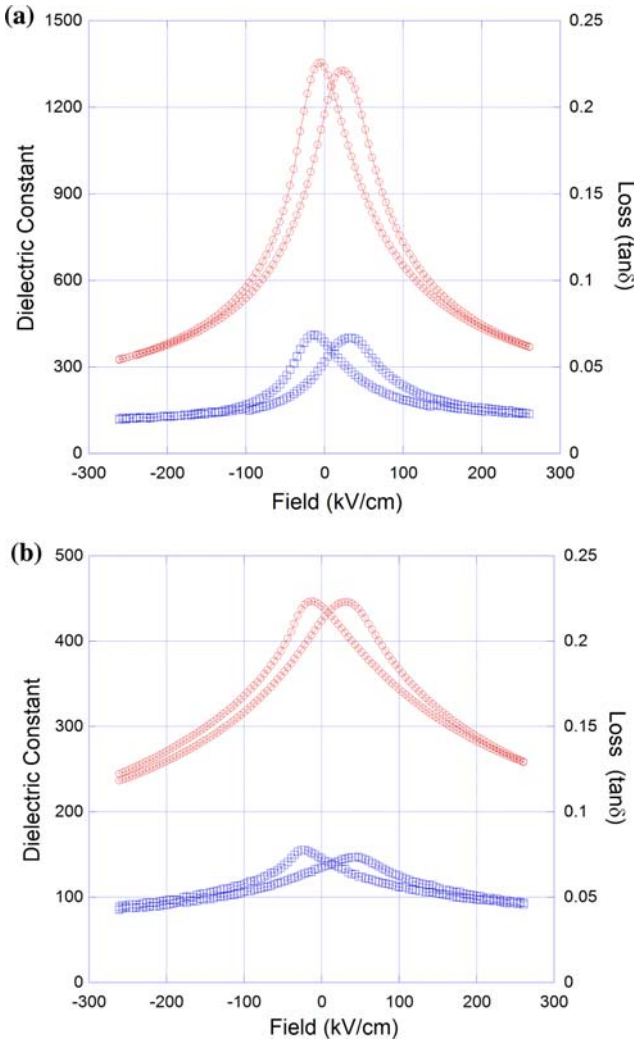

Fig. 4 Dielectric properties measured at room temperature as a function of bias field for: **a** PLZT/LNO/HC and **b** PLZT/HC samples (*circles*, dielectric constant; *squares*, dielectric loss)

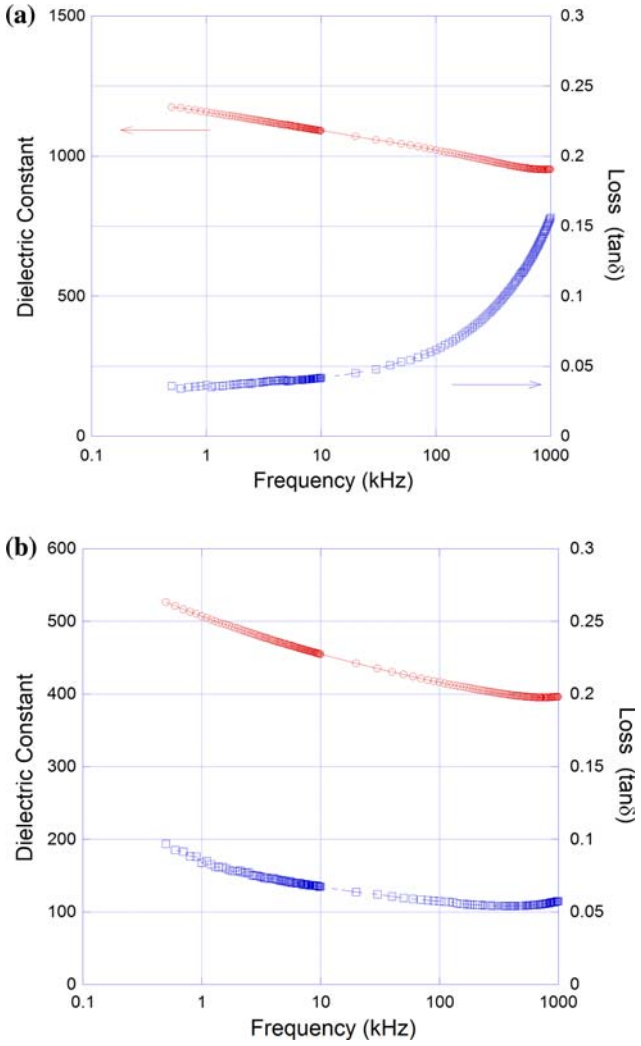

Fig. 5 Dielectric properties measured at room temperature as a function of frequency for: **a** PLZT/LNO/HC and **b** PLZT/HC samples (*circles*, dielectric constant; *squares*, dielectric loss)

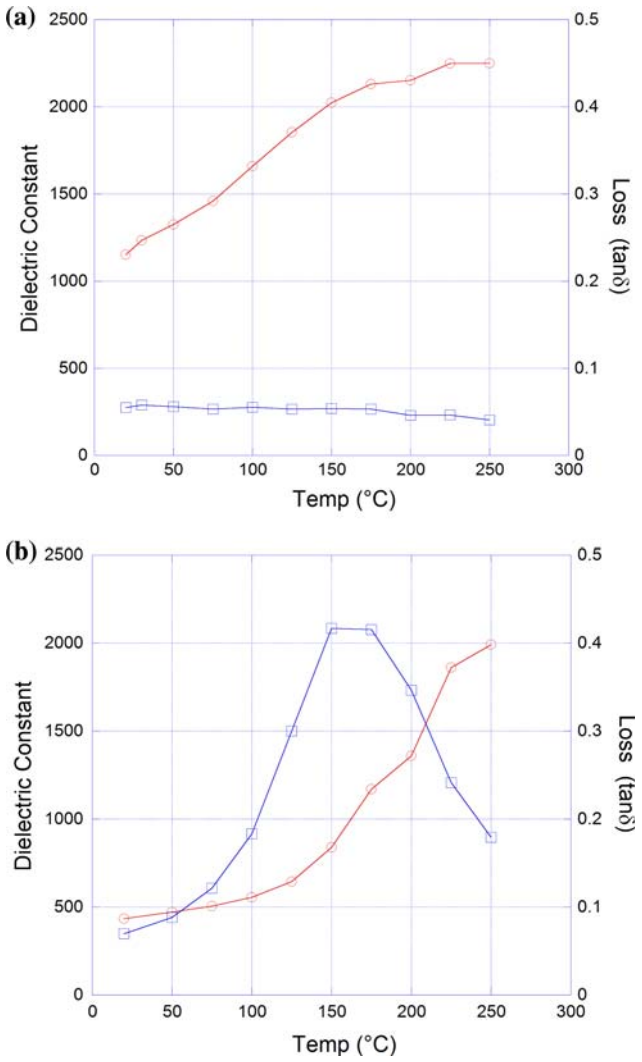

Fig. 6 Dielectric properties measured at various temperatures for: **a** PLZT/LNO/HC and **b** PLZT/HC samples (*circles*, dielectric constant; *squares*, dielectric loss)

HC samples. For PLZT/LNO/HC, the dielectric constant increases and loss decreases with increasing temperature, as shown in Fig. 6a. At 150 °C, a dielectric constant of ≈2,000 and dielectric loss of ≈0.05 were observed. For PLZT/HC, the dielectric constant increases with increasing temperature, while the dielectric loss peaks at ≈160 °C, as shown in Fig. 6b. At 150 °C, dielectric constant of ≈900 and dielectric loss of 0.41 were measured for the PLZT/HC sample. The Curie temperature for PLZT 8/52/48 bulk material was reported between 150 and 190 °C [1]. However, in the dielectric constant data, we did not observe any peaks associated with the phase transition in the temperature range from room temperature to 250 °C. This shift of dielectric constant peak to higher temperature is likely due to the stress inside the PLZT films. Similar behaviors were reported by Kim et al. [20] and Narayanan et al. [21] for PLZT films grown on base metal foils.

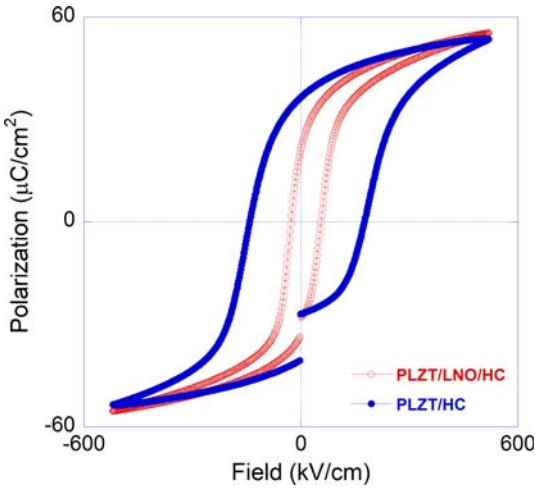

Fig. 7 *P–E* hysteresis loops for PLZT/LNO/HC and PLZT/HC samples

Figure 7 shows the polarization–field (*P–E*) loops measured on PLZT/LNO/HC and PLZT/HC samples with a field sweeping frequency of 1 kHz and maximum applied voltage of 60 V (corresponding to electric field of 521 kV/cm). Both samples have comparable values of spontaneous polarization (P_s). Compared to PLZT/HC, however, the PLZT/LNO/HC sample exhibits a much slimmer *P–E* hysteresis loop, which is desirable for energy storage applications. The remanent polarization (P_r) values were measured to be 21.3 and 36.4 μC/cm^2, while the coercive electric field (E_c) values were determined to be 41 and 173 kV/cm for the PLZT/LNO/HC and PLZT/HC samples, respectively. Our results are comparable to those reported [15] for the PZT (53/47) films grown on HC substrates by solution deposition with and without a conductive oxide buffer.

Figure 8 shows time relaxation data for the current density measured on PLZT/LNO/HC and PLZT/HC samples with Pt top electrodes. A positive voltage of 10 V was applied (corresponding to a field of 87 kV/cm) between the top and bottom electrodes. The decay in dielectric relaxation current obeys the Curie–von Schweidler law [18],

$$J = J_s + J_0 \cdot t^{-n} \quad (1)$$

where J_s is the steady-state leakage current density, J_0 is a fitting constant, t is relaxation time, and n is the slope of the log–log plot. The steady-state leakage current density was determined by fitting the time relaxation data to Eq. 1. Values of $\approx 1.1 \times 10^{-8}$ and $\approx 1.6 \times 10^{-7}$ A/cm^2 were calculated from measurements at room temperature with a bias field of 87 kV/cm for the PLZT/LNO/HC and PLZT/HC samples, respectively.

Figure 9 shows a *P–E* hysteresis loop measured on a PLZT/LNO/HC sample with a field sweeping frequency of 1 kHz. This measurement was conducted with a maximum

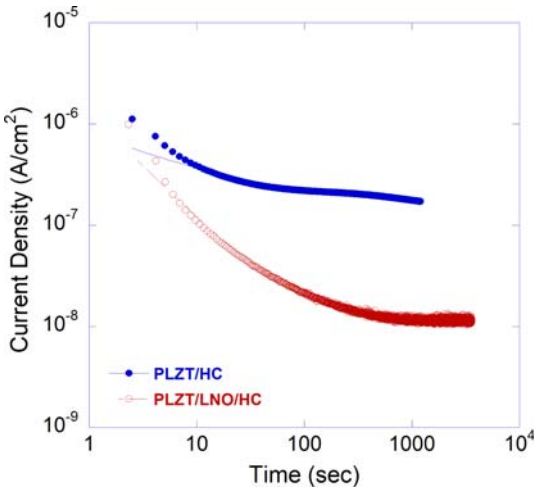

Fig. 8 Time-relaxation current density measured for PLZT/LNO/HC and PLZT/HC samples

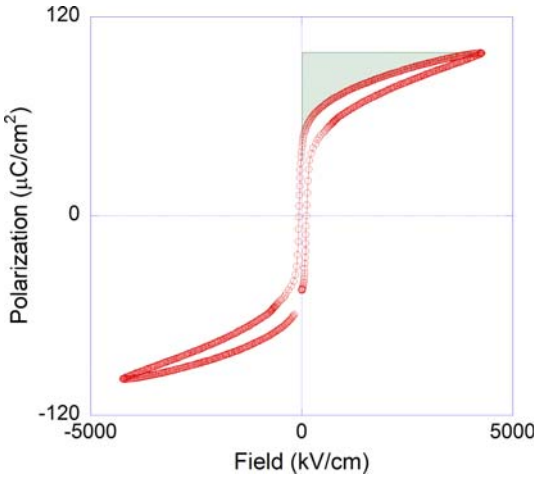

Fig. 9 *P–E* hysteresis loops of PLZT/LNO/HC measured with high applied field. The shaded area indicates energy density that could be recovered from the capacitor

applied voltage of 500 V (corresponding to a field of 4.35×10^6 V/cm). We have observed that remanent polarization increases with increasing applied field. A remanent polarization $P_r = 39.7$ μC/cm^2 was observed from this *P–E* hysteresis loop. Higher value of P_r is possibly due to fast field sweeping frequency used during the measurements. Numerical integration of the discharging portion of the *P–E* hysteresis curve led to a recoverable energy density of ≈65 J/cm^3 in the PLZT/LNO/HC film capacitor, as shown by the shaded area in Fig. 9. This energy density is ≈40% higher than that reported for the PLZT film capacitor grown on nickel foils [12]. Our results demonstrate that PLZT film-on-foil capacitors can potentially be used for high-field energy storage applications.

Conclusions

FE PLZT films were grown on HC substrates by chemical solution deposition with and without an LNO buffer. Samples with the LNO buffer exhibited high dielectric constants and low dielectric loss. At room temperature and zero-bias field, a dielectric constant of ≈1,300 and a dielectric loss of ≈0.06 were measured for the PLZT/LNO/HC sample; the corresponding values were ≈450 and ≈0.07 for the PLZT/HC sample. For the PLZT/LNO/HC sample, the dielectric constant increased and the dielectric loss decreased with increasing temperature. A dielectric constant of ≈2,000 and loss of ≈0.05 were observed at 150 °C. The PLZT/LNO/HC sample exhibited slimmer hysteresis loops and lower leakage current density. The following measurements were made at room temperature under a 87 kV/cm field for PLZT/LNO/HC and PLZT/HC samples: remanent polarization (P_r) values of 21.3 and 36.4 μC/cm^2, the coercive electric field (E_c) values of 41 and 173 kV/cm; leakage current density values of $\approx 1.1 \times 10^{-8}$ and $\approx 1.6 \times 10^{-7}$ A/cm^2, respectively. The energy density of the PLZT/LNO/HC sample was ≈65 J/cm^3. Our results demonstrate that PLZT film-on-foil capacitors can potentially be used for high-field energy storage.

Acknowledgements This work was funded by the U.S. Department of Energy, Office of Vehicle Technologies Program, under Contract DE-AC02-06CH11357. This work benefited from the use of the Electron Microscopy Center (EMC) at Argonne National Laboratory. The authors would like to thank Dr. R. E. Koritala at EMC for her help with scanning electron microscopy. Authors also like to thank Dr. Selvamanickam at IGC-SuperPower for providing HC substrates.

References

1. Haertling GH, Land CE (1971) J Am Ceram Soc 54:1
2. Xia F, Yao X (1999) J Mater Sci 34:3341. doi:10.1023/A:1004672813514
3. Uchiyama K, Kasamatsu A, Otani Y, Shiosaki T (2007) Jpn J Appl Phys 46:L244
4. Guttler B, Bismayer U, Groves P, Salje E (1995) Semicond Sci Technol 10:245
5. Ma B, Kwon DK, Narayanan M, Balachandran U (2008) Mater Lett 62:3573
6. Kandasamy S, Ghantasala MK, Holland A, Li YX, Bliznyuk V, Wlodarski W, Mitchell A (2008) Mater Lett 62:370
7. Ihlefeld J, Laughlin B, Hunt-Lowery A, Borland W, Kingon A, Maria JP (2005) J Electroceram 14:95
8. Kingon AI, Srinivasan S (2005) Nat Mater 4:233
9. Zhao H-J, Ren T-L, Zhang N-X, Zuo R-Z, Wang X-H, Liu L-T, Li Z-J, Gui Z-L, Li L-T (2003) Mater Sci Eng B99:195
10. Kong LB, Ma J (2002) Mater Lett 56:30
11. Seveno R, Gundel HW, Seifert S (2001) Appl Phys Lett 79:4204
12. Ma B, Narayanan M, Balachandran U (2009) Mater Lett 63:1353
13. Ma B, Kwon DK, Narayanan M, Balachandran U (2009) Mater Res Bull 44:11

14. Narayanan M, Kwon DK, Ma B, Balachandran U (2008) Appl Phys Lett 92:252905
15. Seifert S, Sporn D, Hauke T, Muller G, Beige H (2004) J Eur Ceram Soc 24:2553
16. Zou Q, Ruda HE, Yacobi BG (2001) Appl Phys Lett 78:1282
17. Ma B, Kwon DK, Narayanan M, Balachandran U (2009) J Electroceram 22:383
18. Jonscher K (1983) Dielectric relaxation in solids. Chelsea Dielectrics Press, London
19. Chen J, He L, Che L, Meng Z (2006) Thin Solid Films 515:2398
20. Kim T, Hanson JN, Gruverman A, Kingon AI (2006) Appl Phys Lett 88:262907
21. Narayanan M et al (2009) Appl Phys Lett (to be submitted)